Electronic Supplementary Material (ESI) for Journal of Materials Chemistry A.

Supporting Information

Inverted perovskite/silicon V-shaped tandem solar cell with 27.6%-efficiency via self-assembled monolayer modified nickel oxide layer

Likai Zheng,[a] Yimin Xuan,*[a] Jilei Wang,[ab] Shaojuan Bao,[b] Xianglei Liu,[a] and Kai Zhang[a]

[a] School of Energy and Power Engineering, Nanjing University of Aeronautics and Astronautics, Nanjing 210016, P. R. China.

[b] Jinneng Clean Energy Technology Ltd., Lvliang, Shanxi 032100, P. R. China

* Corresponding author: ymxuan@nuaa.edu.cn (Y. Xuan)

Methods

Materials.

The cesium iodide (CsI), lead iodide (PbI_2), lead bromine ($PbBr_2$), formamidinium iodide (FAI) and methylammonium iodide (MAI) were purchased from Sigma Aldrich. The C_{60}, [6,6]-phenyl-C61-butyric acid methyl ester (PCBM) and bathocuproine (BCP) were purchased from Xi'an Polymer Light Technology Corp. The [2-(9H-Carbazol-9-yl) ethyl] phosphonic Acid (2PACz) was purchased from TCI. The NiO_x nanocrystals are purchased from Beijing HuaMin New Materials Technology Co., Ltd. Solvents N,N-Dimethylformamide (DMF), Dimethyl sulfoxide (DMSO), ethyl acetate (EA) and chlorobenzene (CB) were purchased from Sigma Aldrich. The solvent ethanol was purchased from Sinopharm Chemical Reagent Co., Ltd.

Preparation of substrates.

The IWO glass substrates (2.5×2.5 cm^2, ~17 ohm/sq) were cleaned through ultrasonic bath in detergent water, deionized water and ethanol for 20 min, respectively. After being dry by nitrogen flow, the substrates were treated by ozone-ultraviolet for 20 min before use. For NiO_x film preparation, 20 mg NiO_x nanocrystals powder was dissolved in 1 mL deionized water, followed by ultrasonic dispersion for 30 min. After filtered through a 0.45 μm polyether sulfone (PES) filter, the aqueous dispersion was spin-coated on the substrate at 3000 rpm for 30 s with accelerated speed of 3000 rpm/s. After that, the substrate was transferred to a hot plate for annealing at 130℃ for 30 min. Then, the as prepared substrate was immediately transferred to a glovebox with inert gas atmosphere. For SAM layer preparation, 0.25 mg/mL 2PACz/ethanol solution was firstly treated by ultrasonic bath for 15 min, and spin-coated on the IWO/NiO_x or IWO glass substrate at 3000 rpm for 30 s with accelerated speed of 3000 rpm/s, followed by 10 min annealing at 100℃. After annealing, the excess 2PACz molecules can be rinsed by dynamically dripping 100-200 μL ethanol onto the substrates 2-3 times at 4000rpm spin-coating process for 30 s [1], but this step shows little effect on the device performance.

Preparation of CsFAMA-based mixed perovskite precursor.

The perovskite precursor (1.4 M) was prepared by dissolving as purchased powder of 0.07 CsI, 0.21 MAI, 1.12 FAI, 0.315 $PbBr_2$ and 1.128 PbI_2 in a mixture solvent of DMF/DMSO (4:1 v/v). Then the precursor was stirred at 60℃ for 4 h, and was filtered through a 0.22 μm polytetrafluoroethylene (PTFE) filter before use.

Preparation of PCBM solution.

The PCBM solution was prepared by dissolving 12 mg PCBM powder in 950 μL CB solvent, followed by stirring at 60℃ for 6 h.

Device fabrication of the inverted perovskite solar cell.

The perovskite precursor was spin-coated on HTLs at 6000 rpm for 30 s with an accelerated speed of 1000 rpm/s in an N_2 glove box. And then 300 μL of EA as anti-solvent was dropped on the substrate 25 s after the starting of spin-coating. After that, the substrate was annealed at 100℃ for 30 min on a hotplate. For C_{60}-based devices, the perovskite substrates were then transferred to a vacuum chamber without exposure to air, and a 25-nm-thick C_{60} film, as well as a 7-nm-thick BCP film, was successively deposited on the substrates by thermal evaporation at a rate of 0.1 Å s^{-1}. For PCBM-based devices, the prepared PCBM solution was spin-coated on the perovskite at 2000 rpm for 30 s. Then, a 7-nm-thick BCP film was deposited on the PCBM by thermal evaporation at a rate of 0.1 Å s^{-1}. Finally, all devices were completed by depositing Ag (120 nm) film as electrode by thermal evaporation at a rate 1 Å s^{-1}.

Device fabrication of the bifacial HIT silicon solar cell

The bifacial HIT SSC (2 cm x 2 cm substrate with 1.1 cm x 1.1 cm active area) was fabricated through a mass-produced process. Briefly, an n-type M6 crystalline silicon (1 0 0) wafer with resistivity of 1–7 Ω·cm was textured by chemical wet etching to form dual-side pyramid-like micro-structures. After cleaning and drying, the textured wafer was transfer to a vacuum chamber for amorphous silicon deposition. After that, a thin layer of intrinsic hydrogenated amorphous silicon (i-α-Si:H) and a thin layer of n-doped hydrogenated amorphous silicon (n-α-Si:H) were consecutively deposition on one side of the textured wafer through PECVD with 13.56 MHz reactor. Then, a thin layer of i-α-Si:H and a thin layer of p-α-Si:H were consecutively deposition on the other side of the wafer. After that, 80-

nm-thick IWO transparent electrode was deposited on each side of the wafer through reactive plasma deposition (RPD) with an area of 1.1 cm x 1.1 cm defined by a metal mask. The device was finished by screen printing silver H-pattern electrodes on each side of the wafer with the same pattern, following by heat treating at 200℃ for 25 min. Finally, a 2 cm x 2 cm cell with a 1.1 cm x 1.1 cm active area in middle of each side was cut by laser from the M6 wafer.

Characterization of solar cells.

The *J-V* curves of the standalone PSCs and HIT SSCs were measured by a Keithley 2400 source meter under AM1.5G illumination with a solar simulator (CROWNTECH, EASISOLAR-160-3A) with a scan rate of 100 mV/s and 50 mV/s, respectively. The intensity of 1000W/m^2 was calibrated by a standard silicon reference solar cell (CROWNTECH). For tandem measurement, the illumination intensity for each sub-cell was calibrated according to the spectral mismatch factor (IEC60904-7:2008). The illuminated area of the PSC devices was defined by a mask of 0.16 cm^2 perpendicular to the incident light at either normal incidence or 45° oblique incidence. The illuminated area of the standalone HIT SSC was defined by a mask of 0.49 cm^2. For tandem measurement, the bifacial HIT cell was filtered by two PSC filters placed 45° to each side of it, fabricated in the same batch of the actual PSCs. The illuminated area of the bifacial HIT solar cell in reflective tandem system was defined by the masks with 0.49 cm^2 apertures perpendicular to the incident light for each side illumination. The EQE spectra were measured by a CROWNTECH system (QTEST HIFINITY 5) and was calibrated by a certified silicon cell (CROWNTECH) before the measurement. During the EQE measurements for the HIT solar cell, the beam size was adjusted to be as large as possible to cover the active area of the HIT solar cell including the metal fingers. The Mott-Schottky measurements of the PSCs were conducted by an electrochemical workstation (ZAHNER, Zennium pro) under sinusoidal voltage with amplitude and frequency of 10 mV and 10 kHz. The EIS measurements of the PSCs were conducted by an electrochemical workstation (ZAHNER, Zennium pro) under 1 sun illumination with aperture area of 0.16 cm^2. The amplitude of the sinusoidal voltage was 10mV and the bias voltage was 1 V.

Materials characterizations.

The profile images and top-view images of the perovskite films and PSCs were obtained by a field-emission scanning electron microscopy (FESEM; ZEISS, Gemini SEM300). The roughness morphology of the surface of the PSCs were obtained by a laser scanning confocal microscope (LSCM; OLYMPUS, LEXT OLS5000). The spectral characteristics were obtained by a UV-Vis-NIR spectrophotometer (PerkinElmer, Lambda 1050+). The X-Ray Diffraction measurements were conducted by an X-ray diffractometer (BRUKER, D8 ADVANCE). The ultraviolet photoelectron spectra were obtained by a photoelectron spectrometer (Thermo Fisher Scientific, EscaLab 250Xi) with a He-discharge lamp ($h\nu$ = 21.22 eV). Steady-state and time-resolved photoluminescence (PL) spectra were obtained by a photoluminescence spectrometer (Edinburgh, FLS-1000). The steady-state PL measurements were conducted with a Xenon lamp light source and the time-resolved PL measurements were conducted with a pulsed diode laser (EPL) light source of 405 nm.

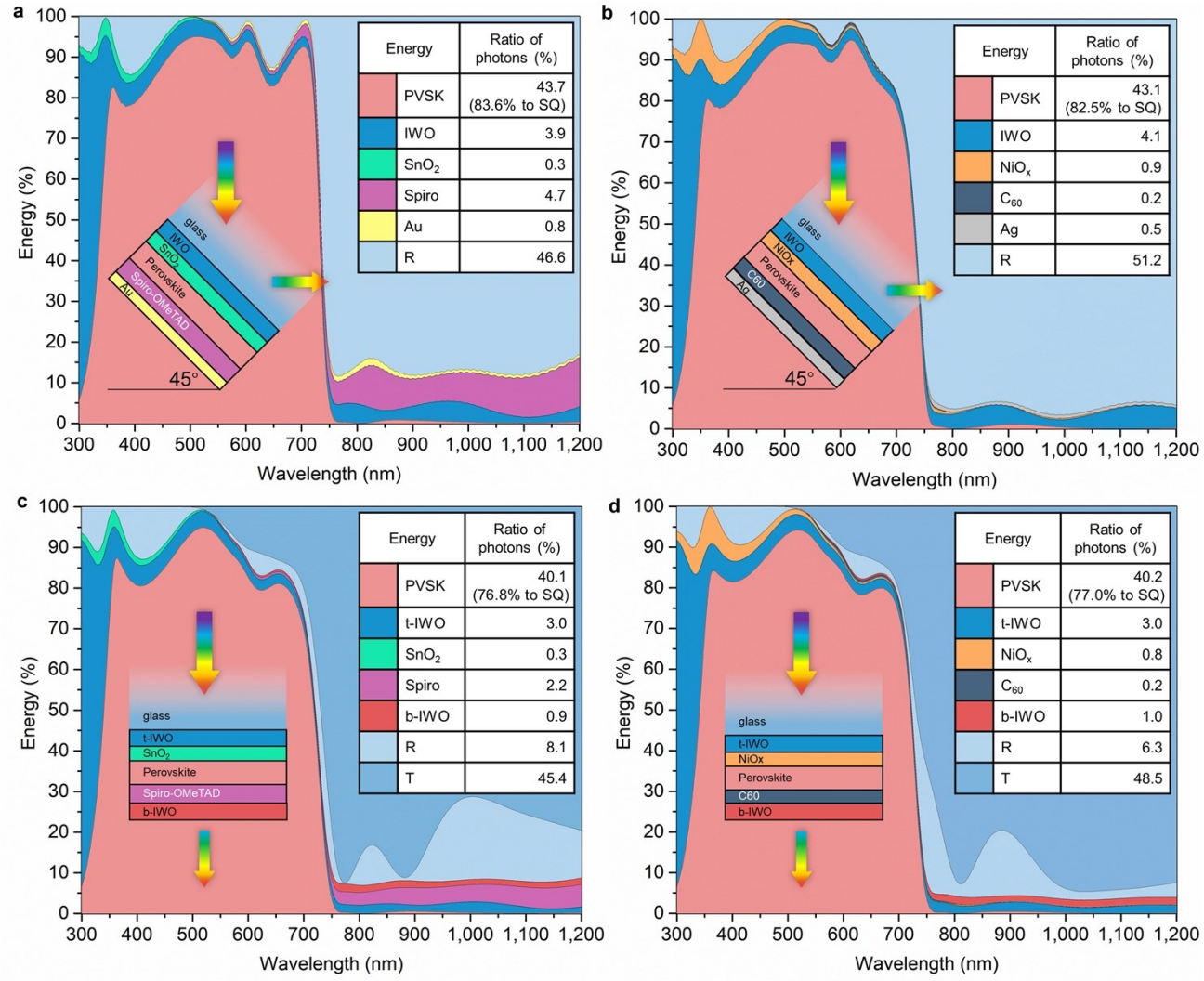

Fig. S1 | Energy distribution in perovskite sub cells with different structures. a, Normal type reflective PSC (glass/IWO (160 nm)/SnO_2 (25 nm)/perovskite (550 nm)/Spiro-OMeTAD (200 nm)/Au (150 nm)) for a V-shaped tandem. b, Inverted type reflective PSC (glass/IWO (160 nm)/NiO_x (25 nm)/perovskite (550 nm)/C_{60} (20 nm)/Ag (150 nm)) for a V-shaped tandem. c, Normal type semitransparent PSC (glass/top-IWO (160 nm)/SnO_2 (25 nm)/perovskite (550 nm)/Spiro-OMeTAD (200 nm)/bottom-IWO (160 nm)) for a mechanically stacked tandem. d, Inverted type semitransparent PSC (glass/top-IWO (160 nm)/NiO_x (25 nm)/perovskite (550 nm)/C_{60} (20 nm)/bottom-IWO (160 nm)) for a mechanically stacked tandem. The simulation models were established based on our previous work [2]. The optical constants (*n, k*) of IWO, SnO_2, NiO_x, perovskite (1.65 eV), Spiro-OMeTAD, and C_{60} were obtained from literatures ref. [2], ref. [3],ref. [4], ref. [5], ref. [6], and ref. [7], respectively. The inset table of each plot represents the ratio of photons attributable to each layer absorption, reflection, and transmission within 300 nm – 1200 nm wavelength range under AM1.5G illumination.

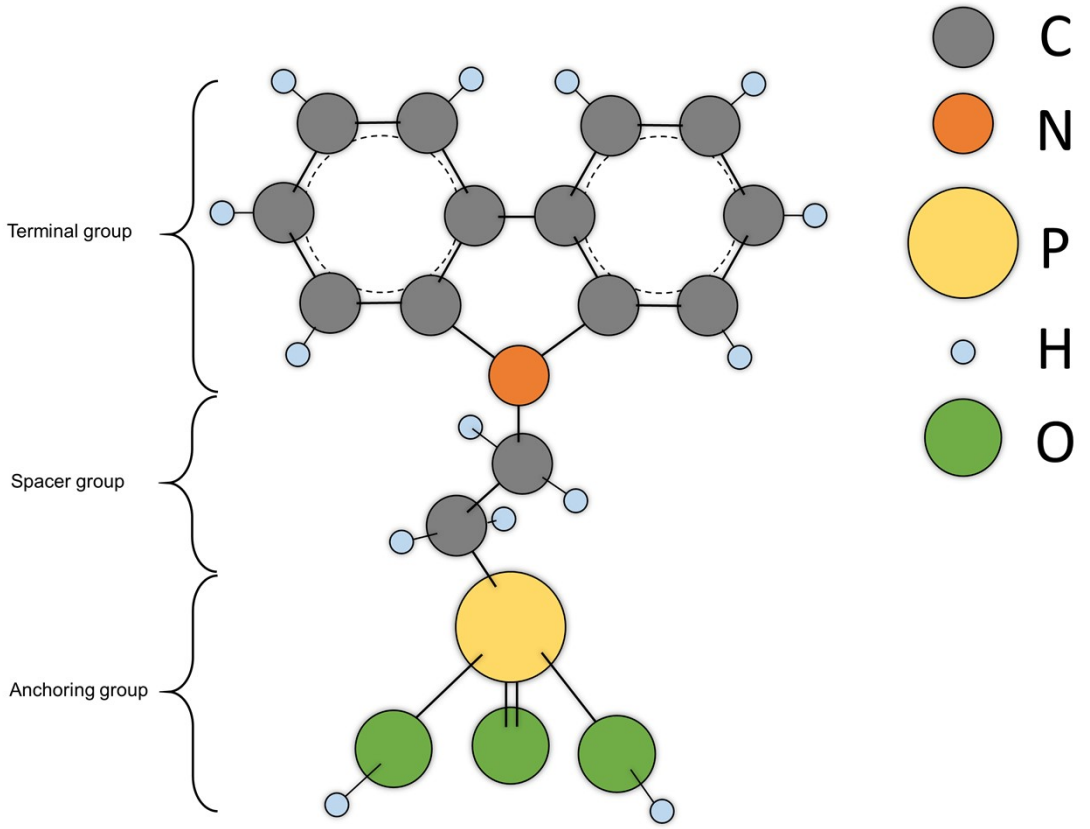

Fig. S2 | The chemical structure of a 2PACz ([2-(9H-carbazol-9-yl) ethyl] phosphonic acid) molecular. The terminal group is carbazole derivative to extract holes from perovskite, and the anchoring group is organic phosphonic acid to bind on the oxide surfaces.

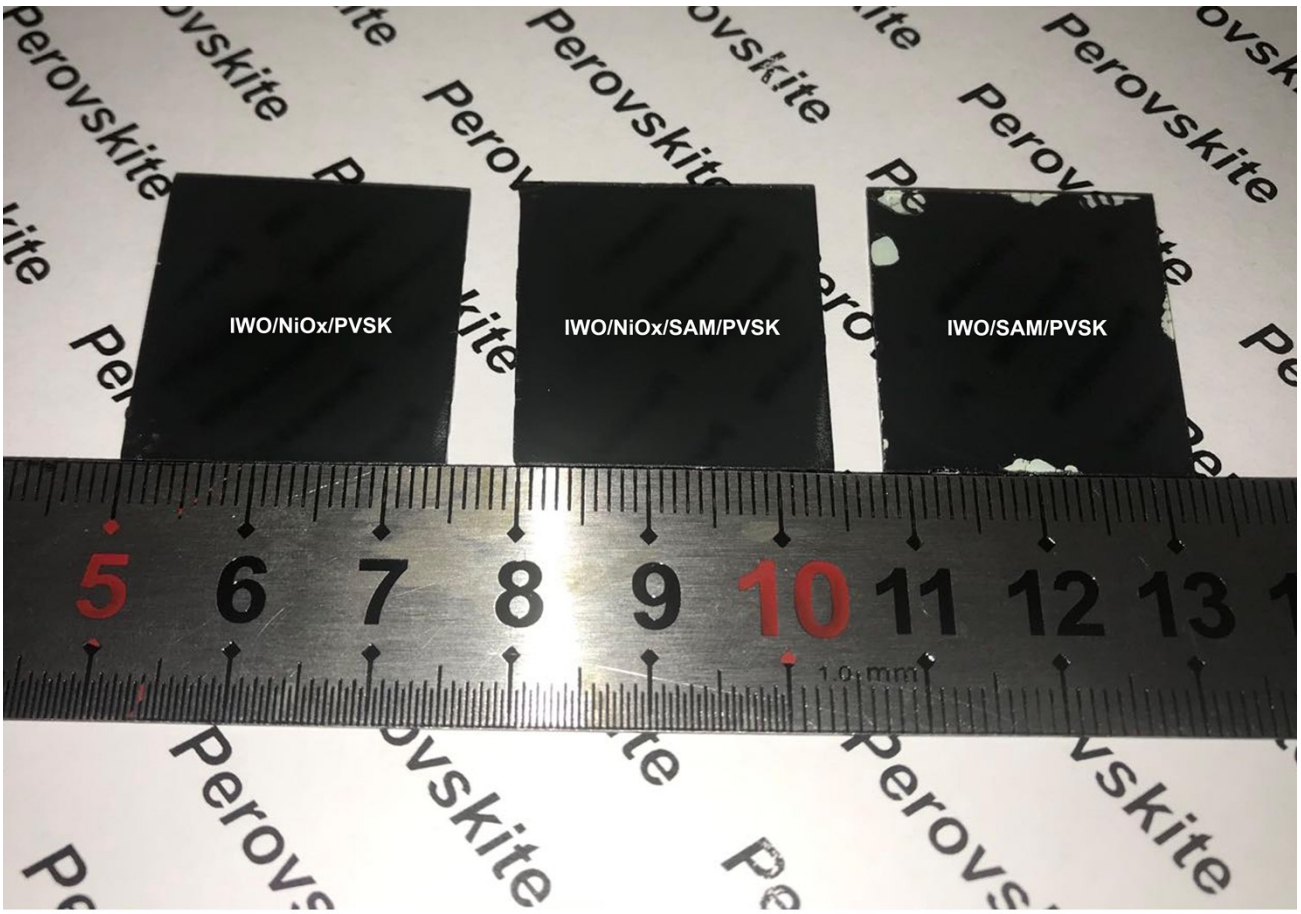

Fig. S3 | Photograph of perovskite films on different substrates. The excellent wetting property of NiO_x layer enables full coverage of perovskite film on IWO/NiO_x and IWO/NiO_x/SAM substrates after spin-coating, while the IWO/SAM substrate is more hydrophobic.

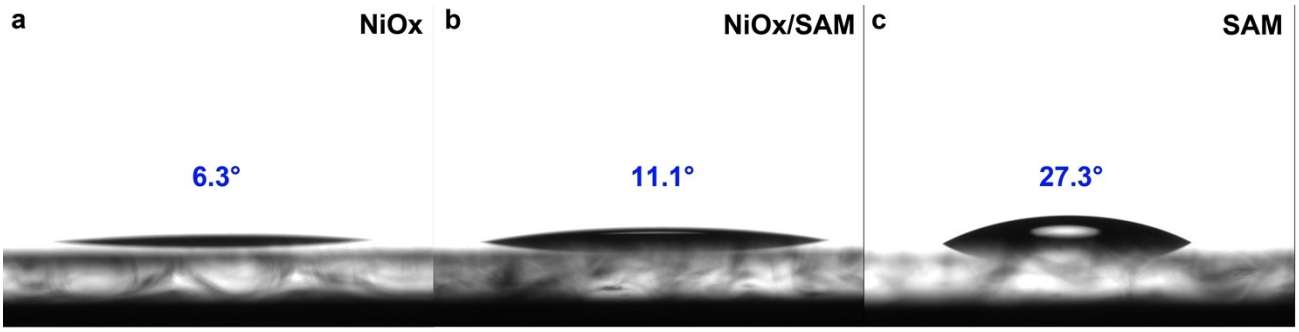

Fig. S4 | Contact angle of perovskite precursor solution on different HTLs. The contact angle on the SAM HTL is much larger than that on the NiO_x and the NiO_x/SAM HTLs, indicating the enhanced wettability by NiO_x films.

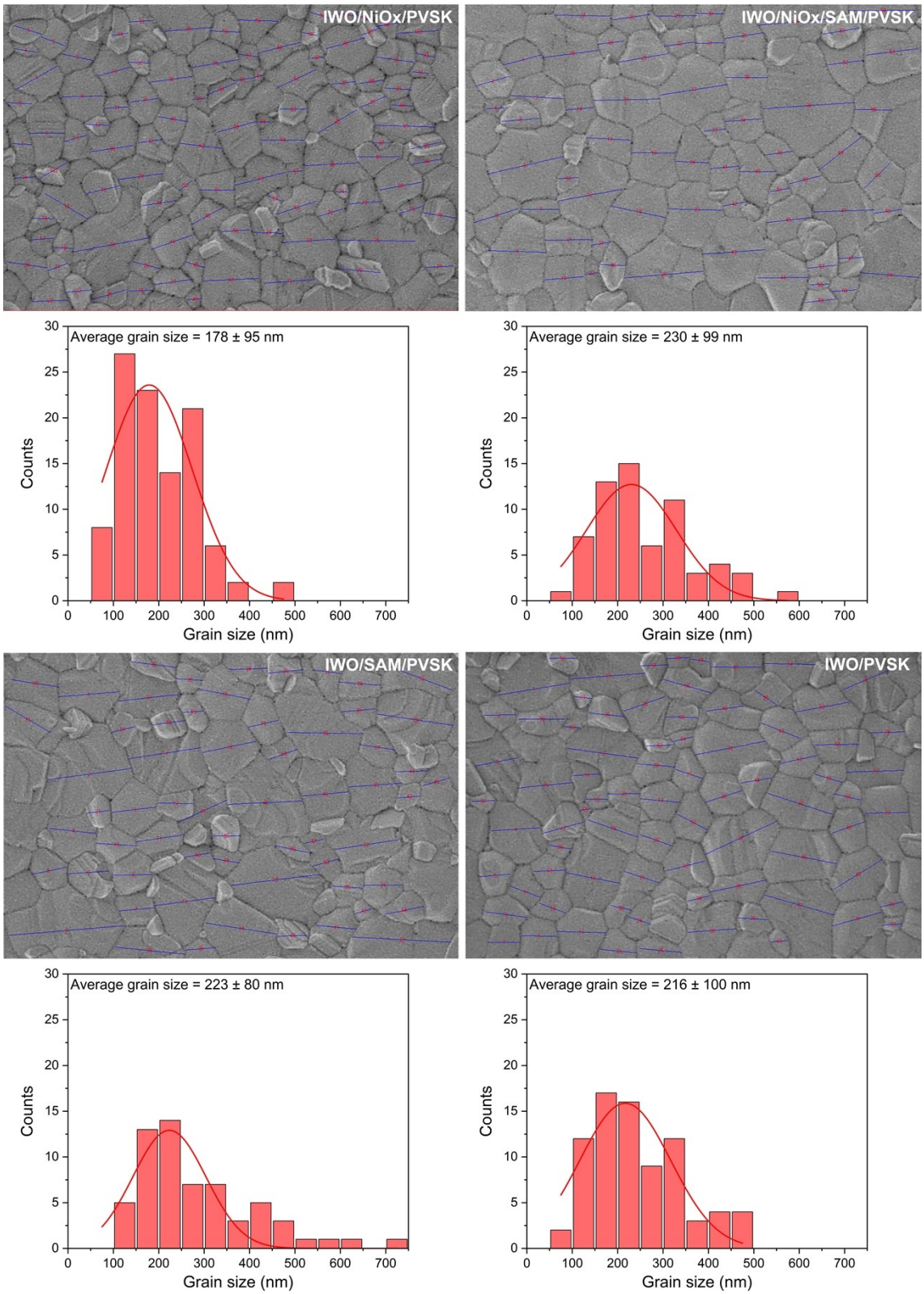

Fig. S5 | Statistical distribution of perovskite grain size of perovskite films on different substrates.

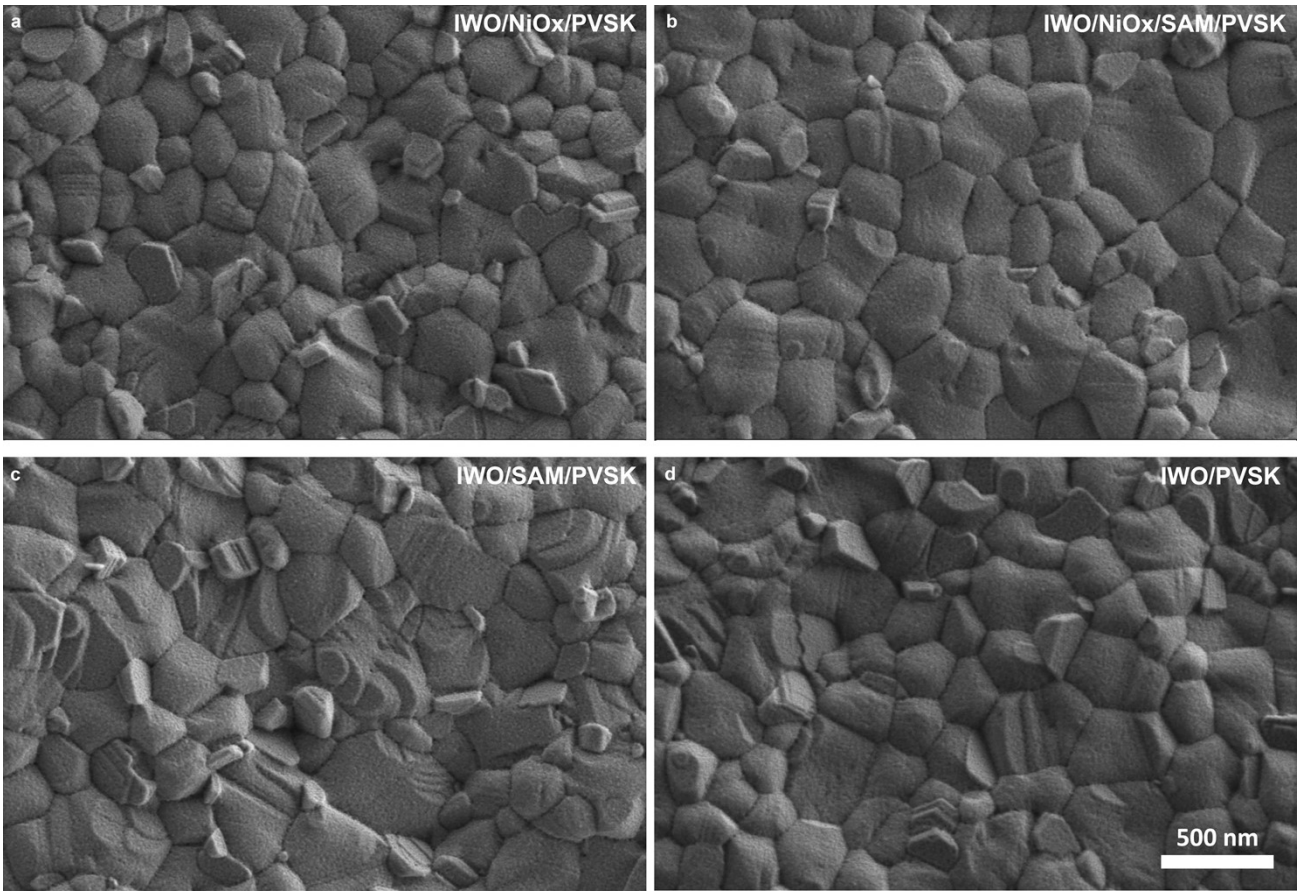

Fig. S6 | Top-view SEM images of perovskite films obtained by the SE2 detector. a, Perovskite film on IWO/NiO_x substrate. b, Perovskite film on IWO/NiO_x/SAM substrate. c, Perovskite film on IWO/SAM substrate. d, Perovskite film on bare IWO substrate. The SE2 detector collects the secondary electrons on the side of the samples to provide stereoscopic morphology images. The perovskite film on IWO/NiO_x/SAM substrate exhibits a smoother surface.

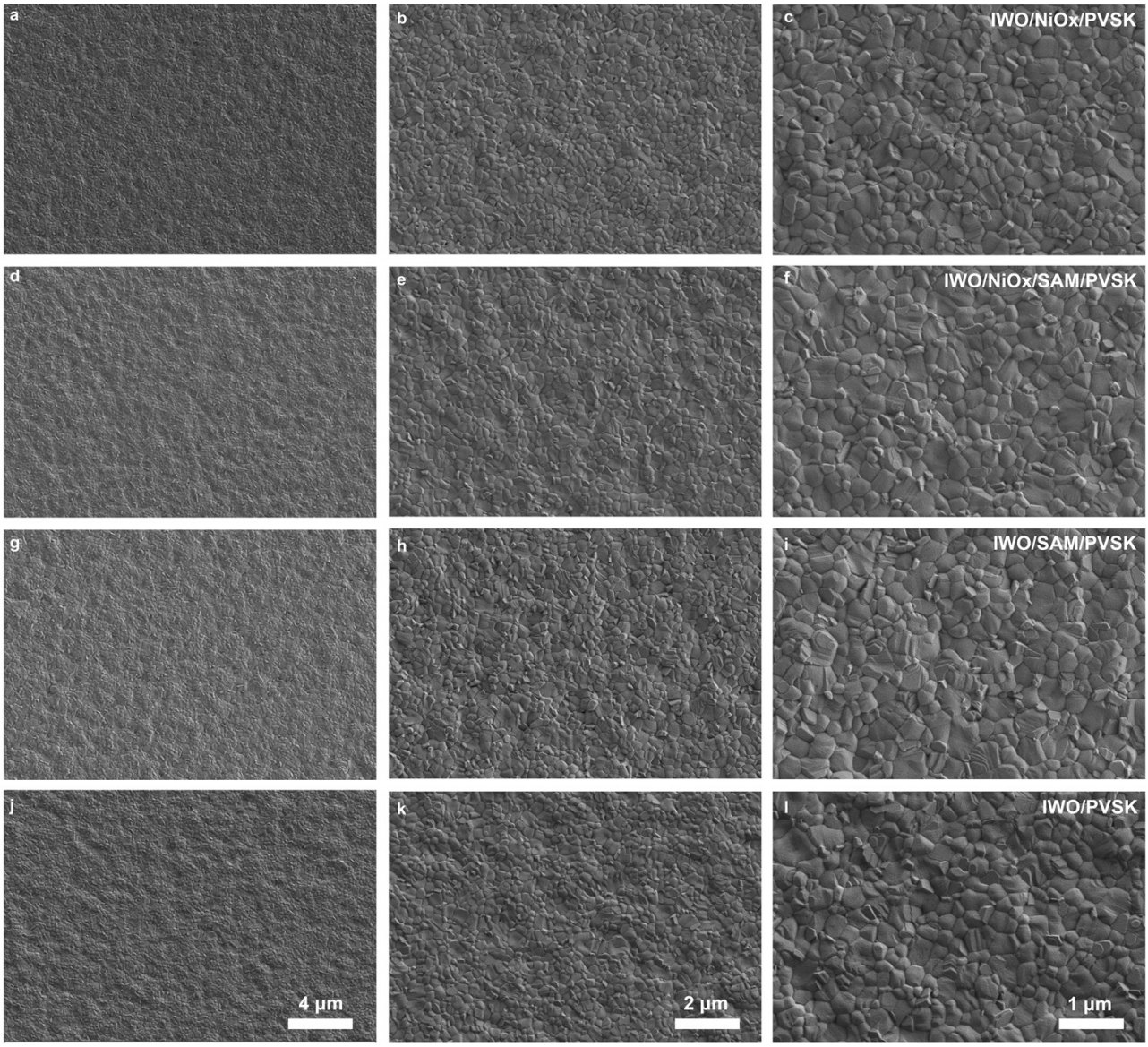

Fig. S7 | Top-view SEM images of perovskite films in different scales obtained by the SE2 detector. a-c, Perovskite film on IWO/NiO_x substrate. d-f, Perovskite film on IWO/NiO_x/SAM substrate. g-i, Perovskite film on IWO/SAM substrate. j-l, Perovskite film on bare IWO substrate.

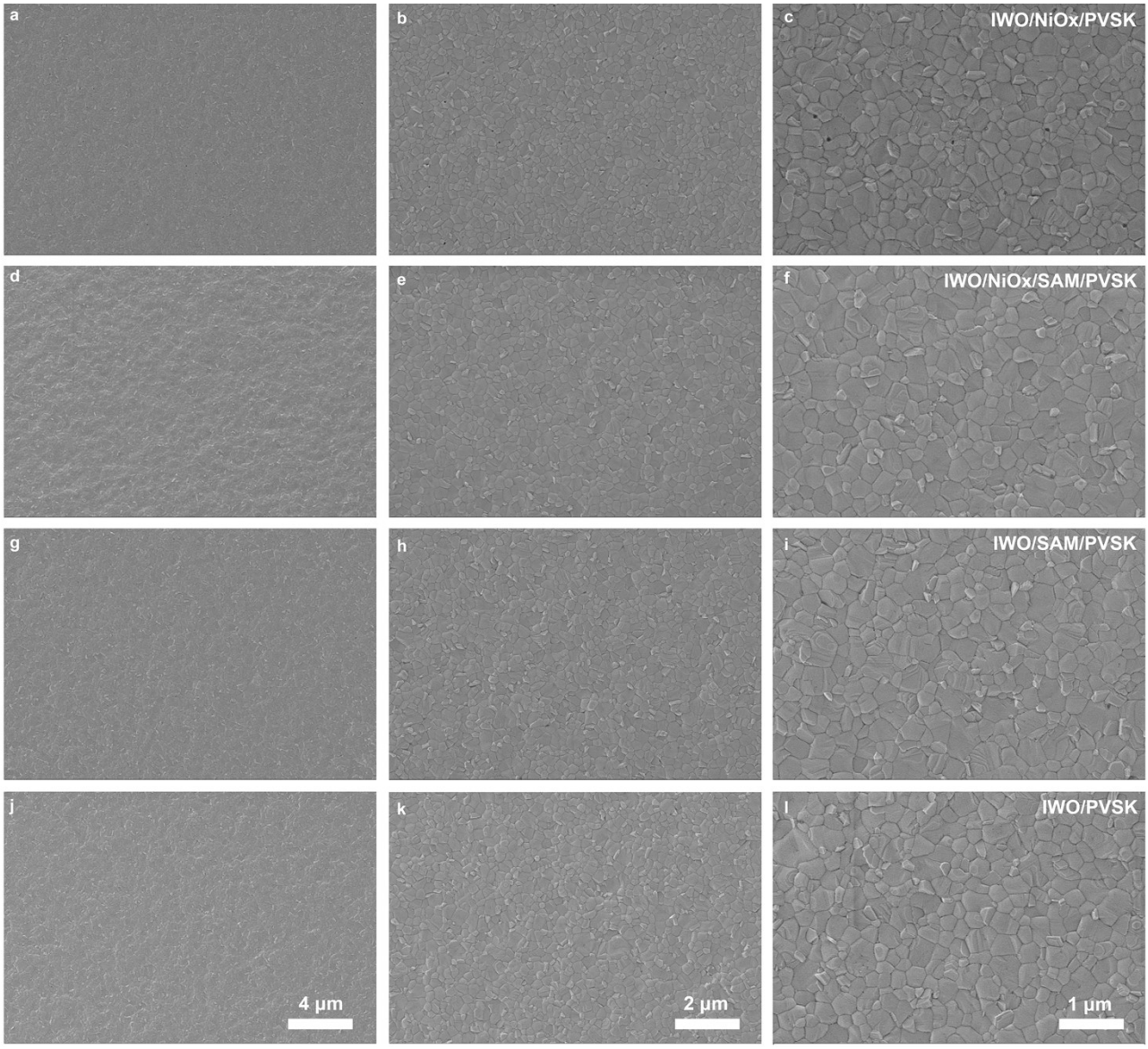

Fig. S8 | Top-view SEM images of perovskite films in different scales. a-c, Perovskite film on IWO/NiO_x substrate. d-f, Perovskite film on IWO/NiO_x/SAM substrate. g-i, Perovskite film on IWO/SAM substrate. j-l, Perovskite film on bare IWO substrate.

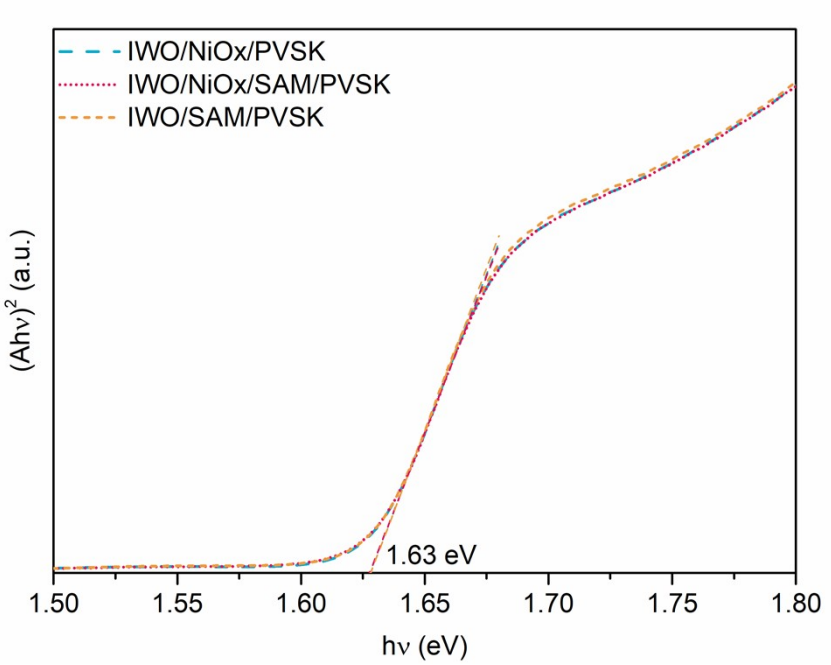

Fig. S9 | Tauc plots of the perovskite films on different HTLs. The perovskite films on three kinds of HTLs exhibit similar bandgap of 1.63 eV.

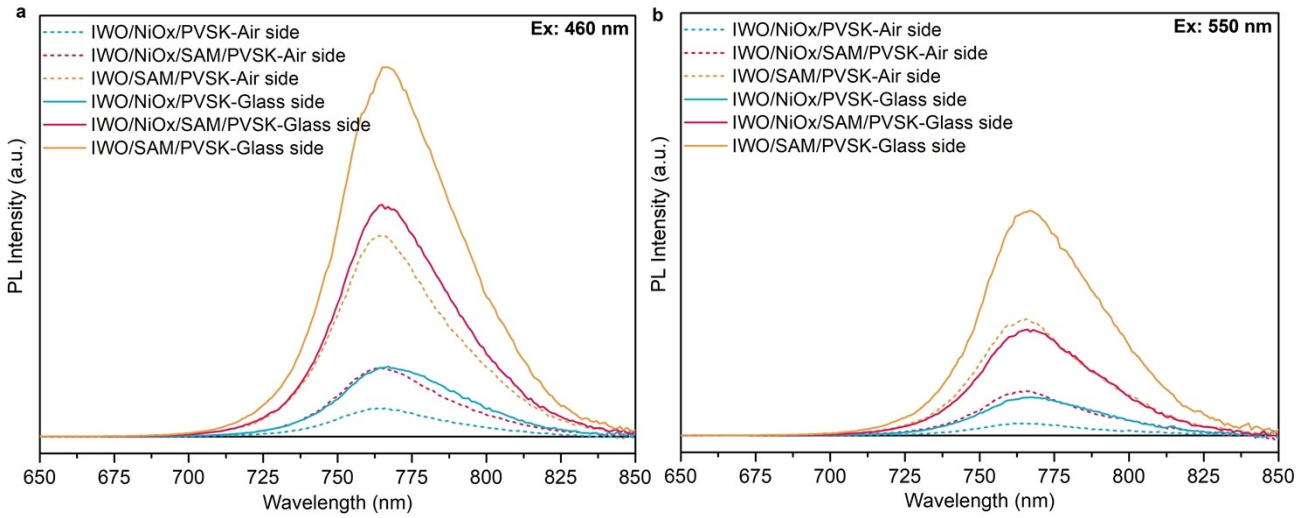

Fig. S10 | Stead-state PL spectra of the perovskite films on different substrates. a, Spectra measured under 460 nm excitation light. b, Spectra measured under 550 nm excitation light.

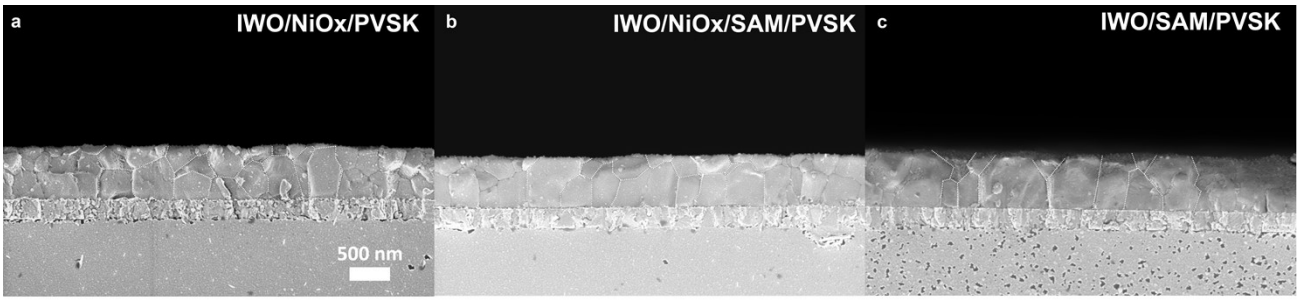

Fig. S11 | Profile SEM images of perovskite films on different substrates. a, Perovskite film on IWO/NiO_x substrate. b, Perovskite film on IWO/NiO_x/SAM substrate. c, Perovskite film on IWO/SAM substrate. The perovskite films on IWO/NiO_x and IWO/NiO_x/SAM substrates shows more grain boundaries (white dash lines) than that on the IWO/SAM substrate.

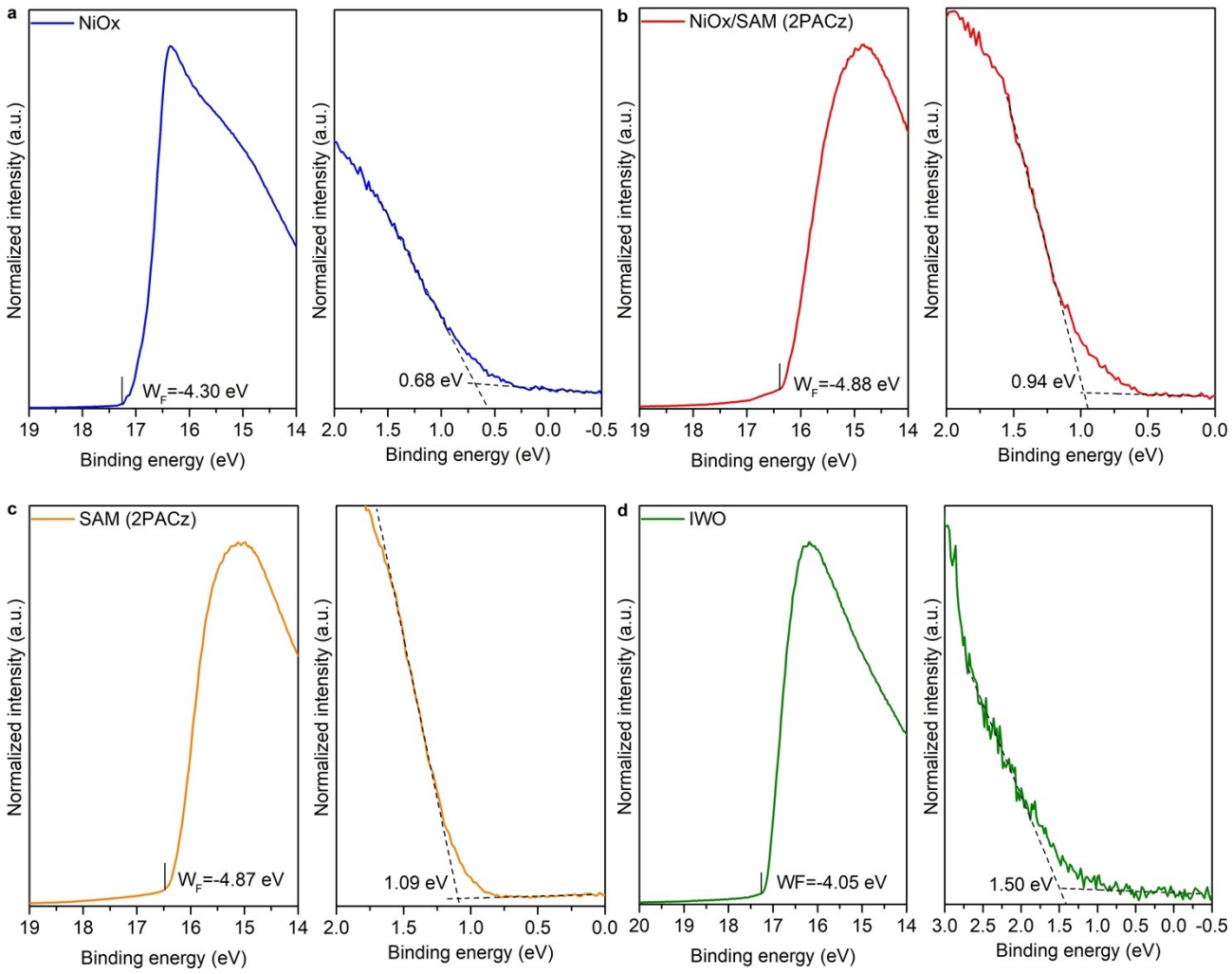

Fig. S12 | Ultraviolet photoelectron spectra (UPS) of different substrates. a, NiO_x film fabricated on IWO. b, NiO_x/SAM film fabricated on IWO. c, SAM film fabricated on IWO. d, IWO film.

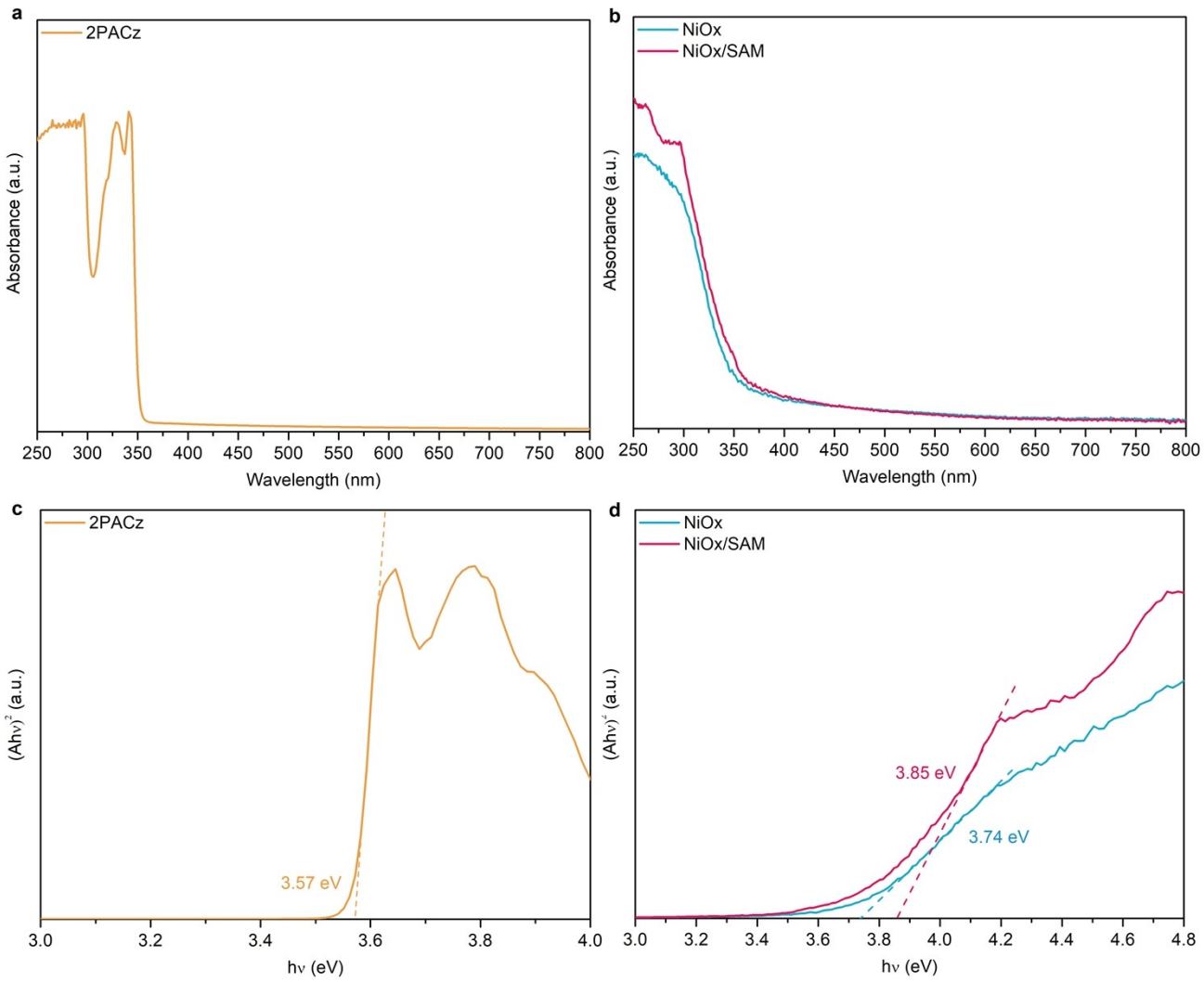

Fig. S13 | Optical absorption properties of different HTLs. a, Absorbance curve of 2PACz solution in ethanol at a concentration of 0.25 mg mL^{-1}. b, Absorbance curves of NiO_x and NiO_x/SAM films on quartz substrates. c, Tauc plot of the 2PACz solution. The bandgap is 3.57 eV. d, Tauc plots of the NiO_x and NiO_x/SAM films. The bandgaps are 3.74 eV and 3.85 eV, respectively.

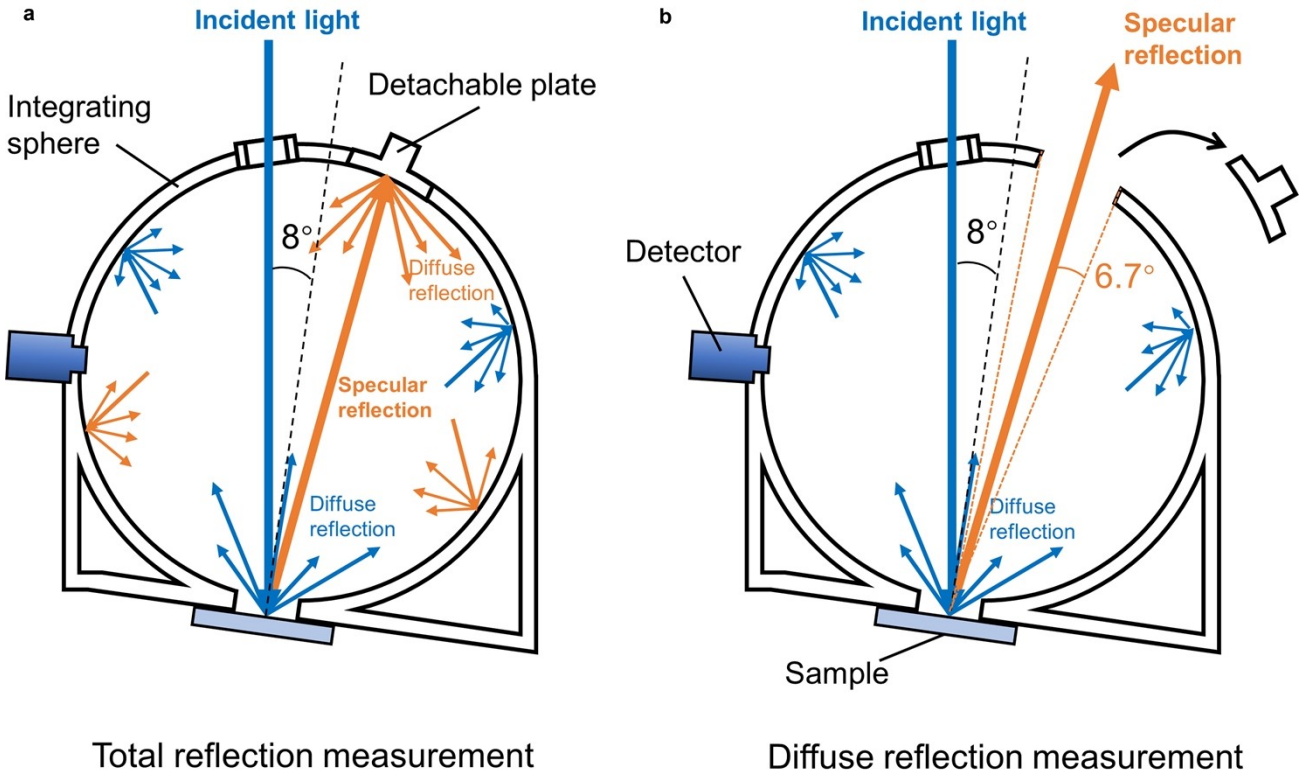

Fig. S14 | Schematic diagrams of reflection measurements with the integrating sphere. a, Total reflection measurement. The sample is placed at an angle of 8 degrees to the incident light. The specular as well as diffuse reflected light is uniformly distributed on the surface of the integrating sphere after multiple reflections inside the sphere, and is then received by the detector. b, Diffuse reflection measurement. Part of the sphere of the integrating sphere is removed. The specular reflected light propagates directly to the outside through this window, while the diffuse reflected light is uniformly distributed on the surface of the integrating sphere after multiple reflections inside the sphere, and is then received by the detector. The diffuse angle is 6.7° defined by the size of window and the distance between the sample and the window.

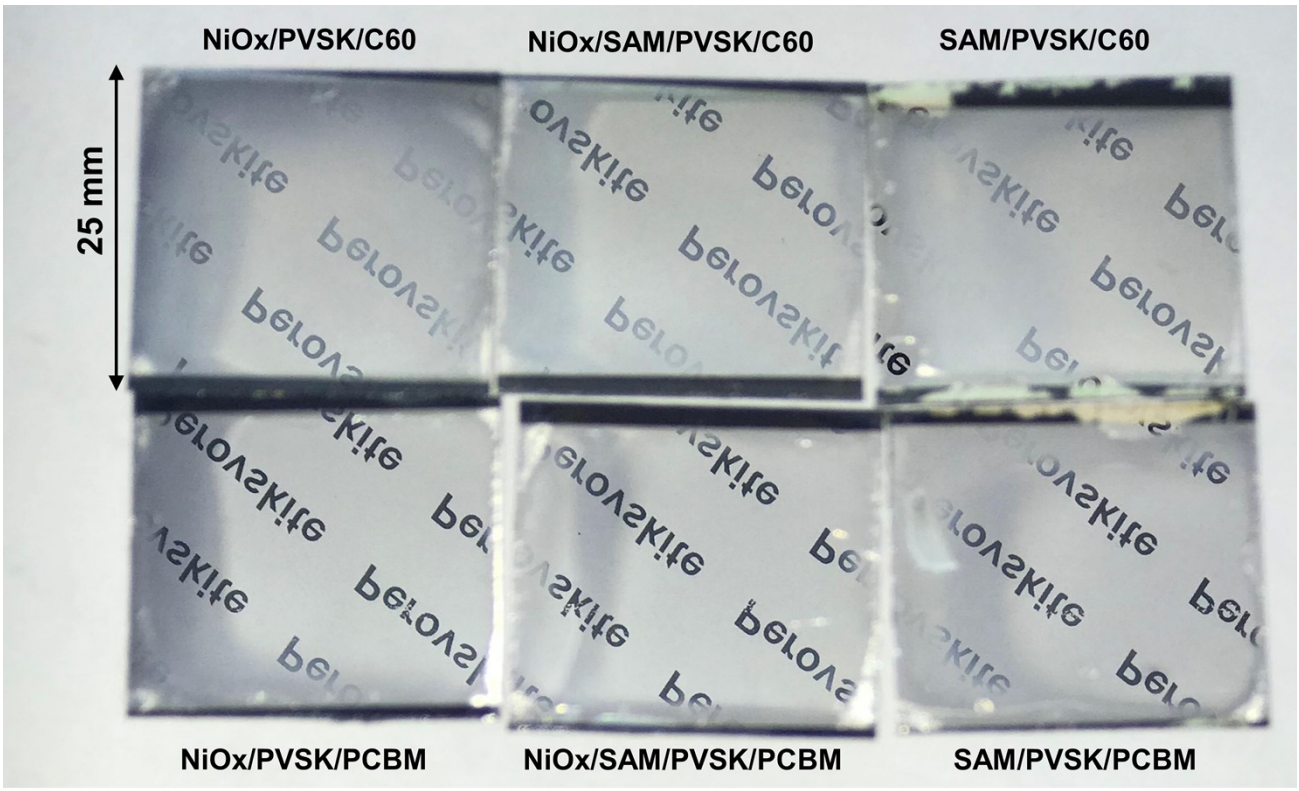

Fig. S15 | Photographs of the Ag electrode side of the PSC filters with different HTLs and ETLs. Compared to the C_{60} ETL, the PCBM ETL significantly improves the smoothness of Ag electrodes.

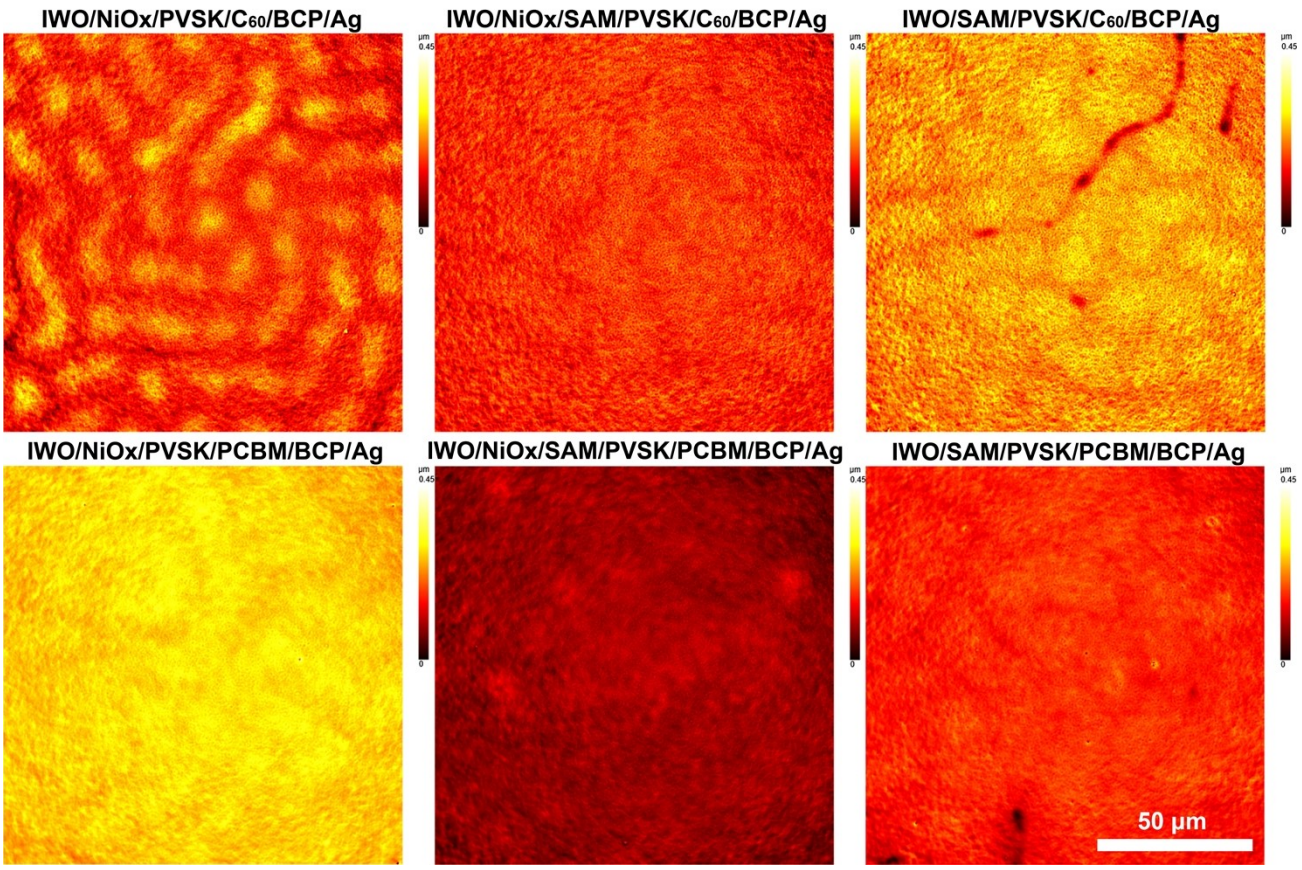

Fig. S16 | Laser scanning confocal microscope (LSCM) images of the Ag electrode side of the PSC filters with different HTLs and ETLs (128 µm x 128 µm area).

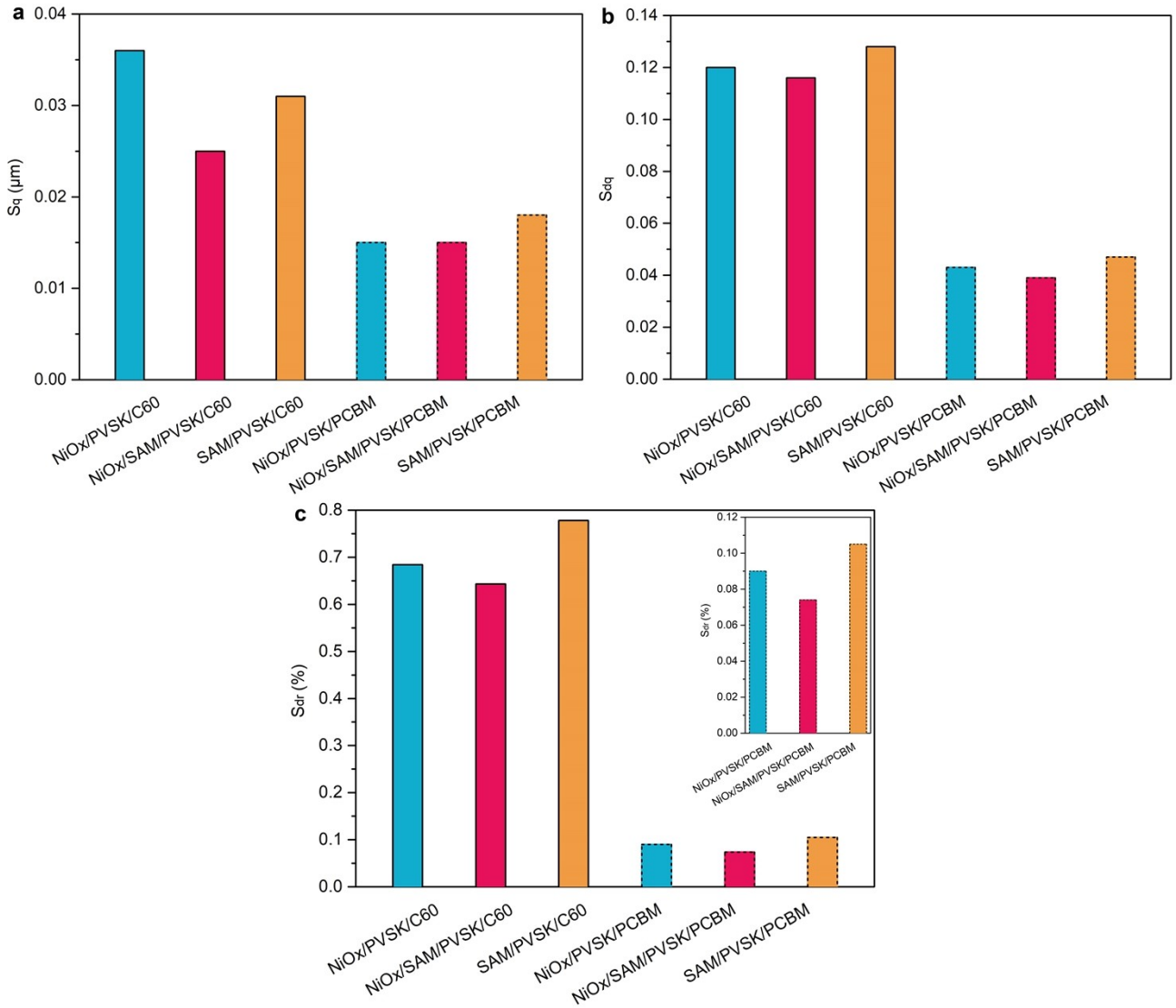

Fig. S17 | The roughness parameters obtained from the LSCM images. a, S_q (surface root mean square height; 128 μm × 128 μm area) b, S_{dq} (surface root mean square gradient; 128 μm × 128 μm area). c, S_{dr} (interface expansion area ratio; 128 μm × 128 μm area).

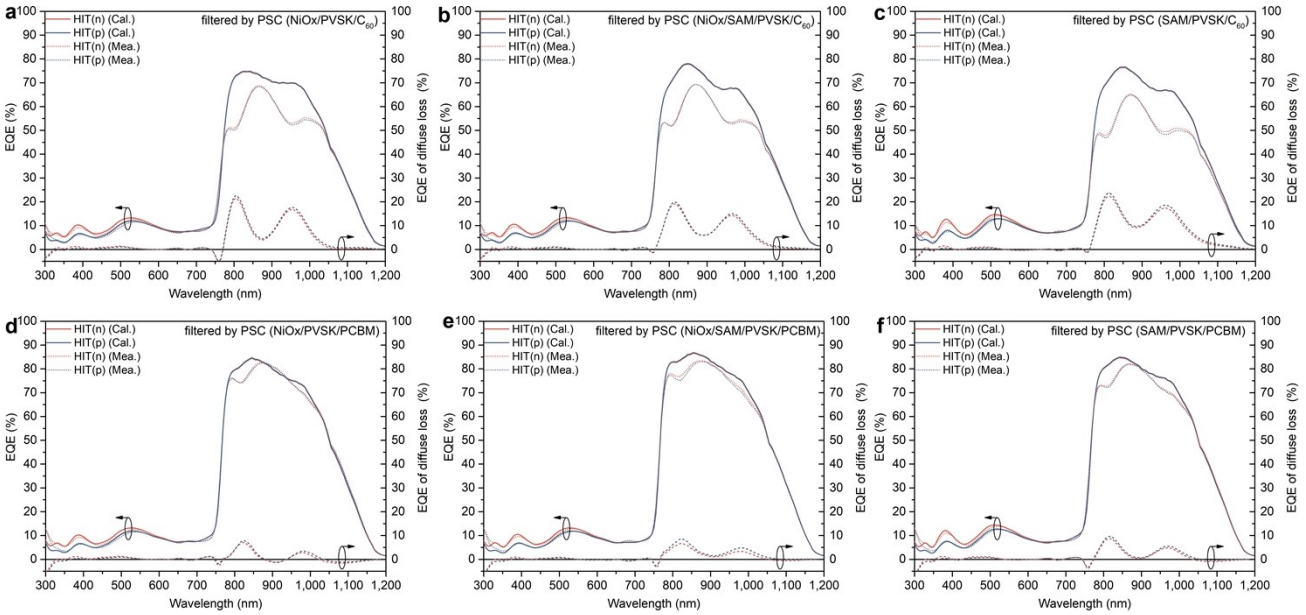

Fig. S18 | Measured EQE spectra, calculated EQE spectra, and EQE of diffuse loss of the rear (p) side of the HIT SSC filtered by PSCs with different ETLs and HTLs. a, HIT SSC filtered by PSC (NiO_x/PVSK/C60). b, HIT SSC filtered by PSC (NiO_x/SAM/PVSK/C60). c, HIT SSC filtered by PSC (SAM/PVSK/C60). d, HIT SSC filtered by PSC (NiO_x/PVSK/PCBM). e, HIT SSC filtered by PSC (NiO_x/SAM/PVSK/PCBM). f, HIT SSC filtered by PSC (SAM/PVSK/PCBM).

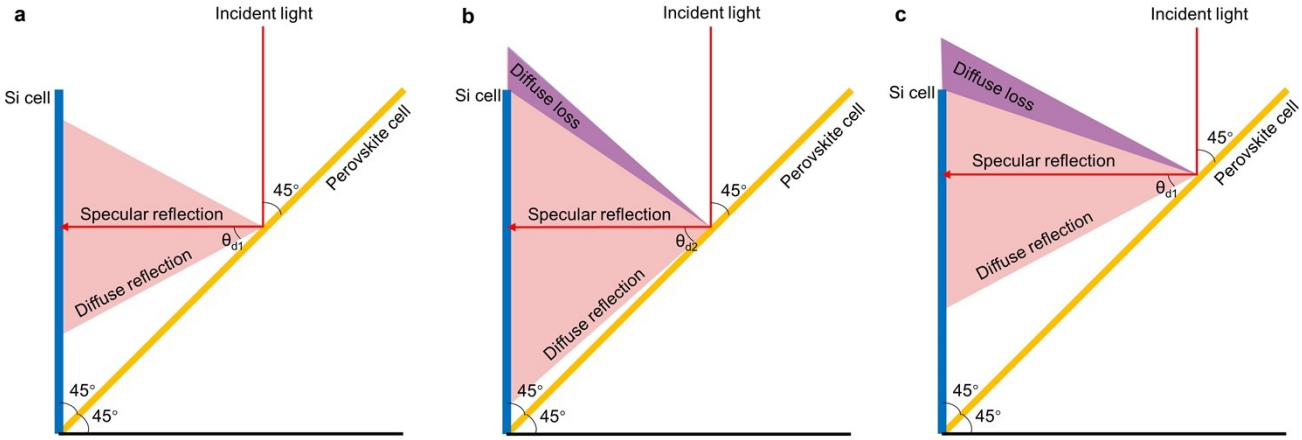

Fig. S19 | Schematic diagrams of the incident and reflected light in a perovskite/silicon V-shaped tandem configuration (one of the sides of the symmetrical structure). a, The specular reflection (red line with an arrow) and the diffuse reflection (pink triangle area; with a diffuse angle of θ_{d1}) from the perovskite cell are fully received by the Si cell. b, The specular reflection (red line with an arrow) and most of the diffuse reflection (pink triangle area; with a diffuse angle of θ_{d2}, $\theta_{d2} > \theta_{d1}$) from the perovskite cell are received by the Si cell. Part of the diffuse reflection (purple triangle area) escapes from the top edge of the Si cell due to the larger diffuse angle, resulting in the diffuse loss. c, The specular reflection (red line with an arrow) and most of the diffuse reflection (pink triangle area; with a diffuse angle of θ_{d1}) from the perovskite cell are received by the Si cell. Part of the diffuse reflection (purple triangle area) escapes from the top edge of the Si cell due to the higher position of the reflection, resulting in the diffuse loss.

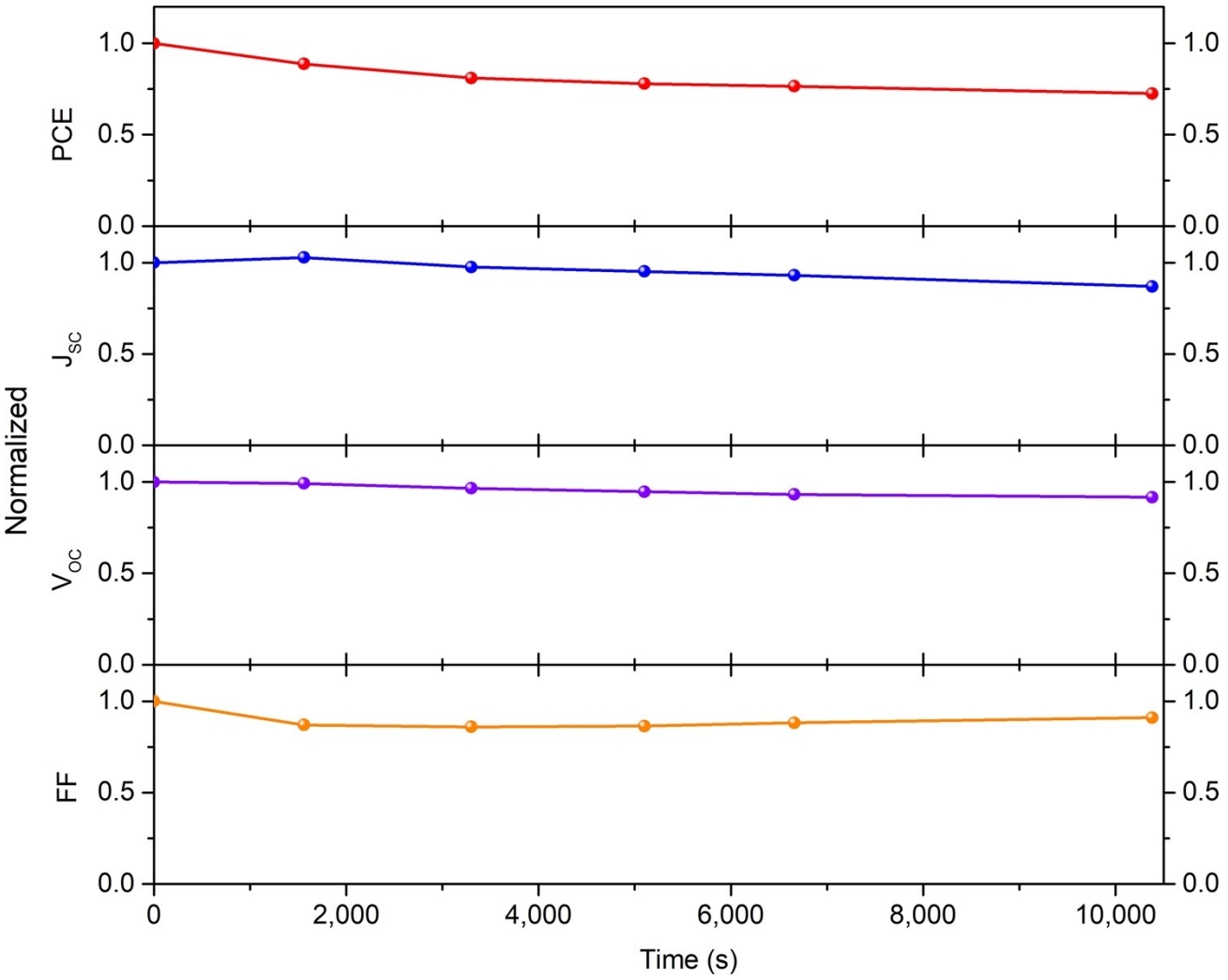

Fig. S20 | Normalized photovoltaic parameters of the PSC with NiO_x/SAM HTL and PCBM ETL obtained from the light soaking and moisture stability measurement. The stability measurement was conducted by continuously exposing the unencapsulated PSC to 1 sun (AM1.5G) illumination (xenon lamp) in an air environment with a relative humidity of 30-40%.

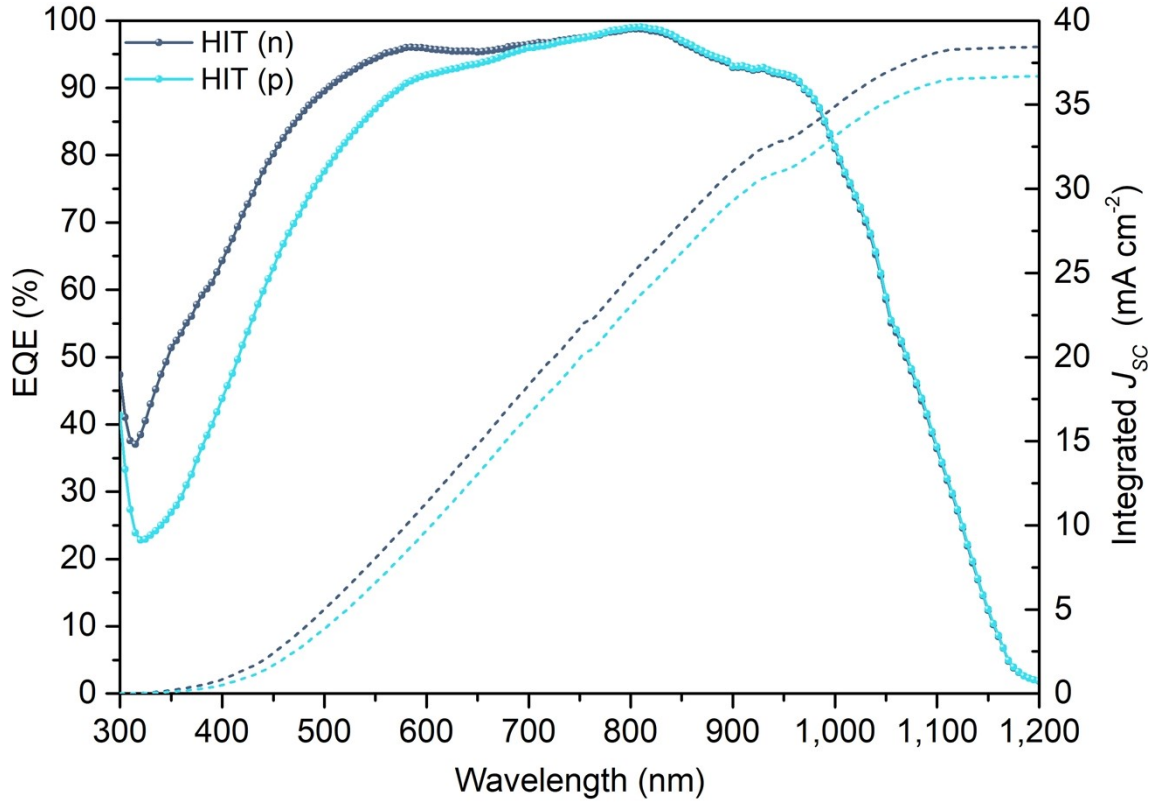

Fig. S21 | EQE spectra of the standalone bifacial HIT SSC under illumination on each side. The integrated JSC are 38.4 mA cm^{-2} and 36.7 mA cm^{-2} for the front (n) side and the rear (p) side, respectively.

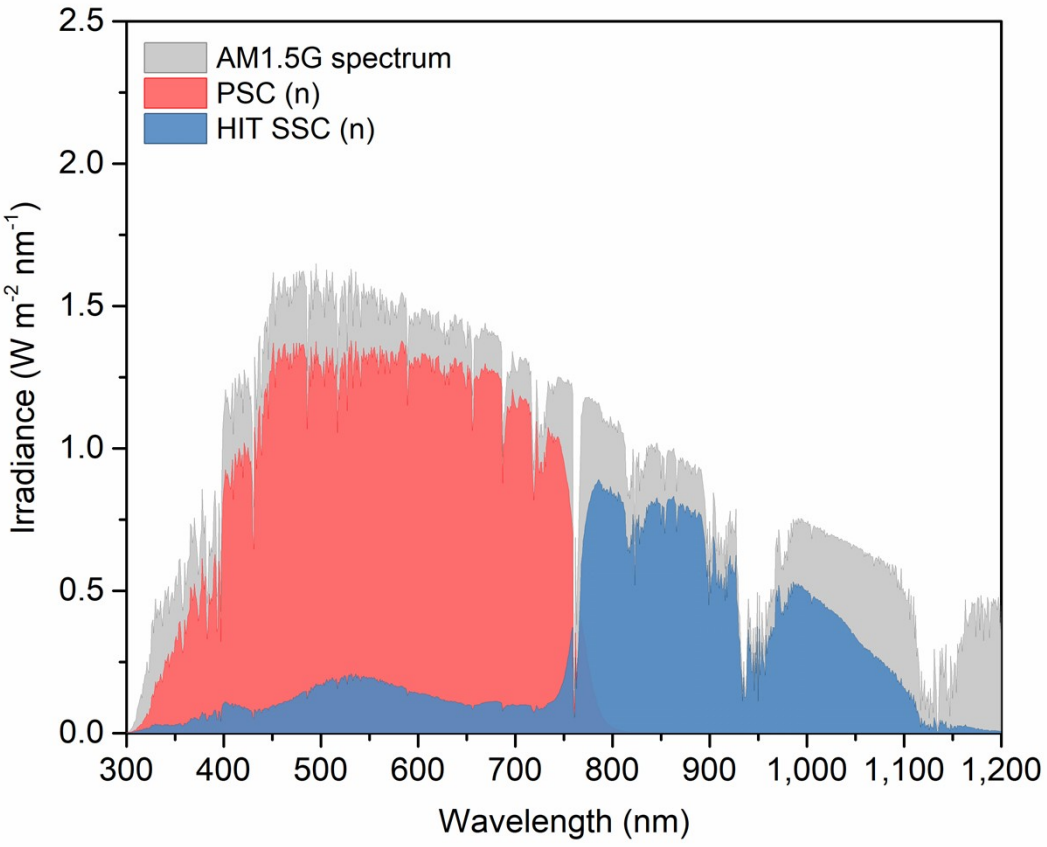

Fig. S22 | Light utilization of solar spectrum by sub-cells.

Table S1 Fitting parameters of the time-resolved PL spectra of perovskite films from glass side.

Sample	B_1 [%]	τ_1 [ns]	B_2 [%]	τ_2 [ns]	Weighted average τ [ns]
IWO/NiO_x/PVSK (Glass side)	0.23	3.10	99.77	644.62	643.14
IWO/NiO_x/SAM/PVSK (Glass side)	0.21	10.22	99.79	907.65	905.77
IWO/SAM/PVSK (Glass side)	0.13	11.32	99.87	952.68	951.45

Table S2 Fitting parameters of the time-resolved PL spectra of perovskite films from air side.

Sample	B_1 [%]	τ_1 [ns]	B_2 [%]	τ_2 [ns]	B_3 [%]	τ_3 [ns]	Weighted average τ [ns]
IWO/NiO_x/PVSK (Air side)	1.25	3.28	2.35	21.29	96.40	912.41	880.14
IWO/NiO_x/SAM/PVSK (Air side)	0.65	3.55	1.78	25.57	97.57	912.97	891.23
IWO/SAM/PVSK (Air side)	0.45	5.18	1.43	209.36	98.12	1559.37	1533.08

Table S3 Fitting parameters of the EIS measured results of the PSCs.

		PSC (NiO_x)	PSC (NiO_x/SAM)	PSC (SAM)
R_S (ohm)		14.5	8.44	28.6
R_1 (ohm)		8.37	12.4	13.1
R_2 (ohm)		182	135	169
R_3 (ohm)		23.8	32.1	48.5
Q_1	C (μF)	189	985	20.1
	exponent	0.602	0.512	0.813
Q_2	C (μF)	114	95.6	45.7
	exponent	1	0.725	0.73
Q_3	C (μF)	25.3	27.9	0.0375
	exponent	0.957	0.853	0.837
L_1 (μH)		3750	25.6	40.9
R_C (ohm)		1.72	9.73	20.7
L_h (nH)		680	770	741
R_h (ohm)		72.4	77	30.2

Table S4 Roughness parameters of the Ag electrode surfaces of PSCs.

Device	S_q (μm)	S_{dq}	S_{dr} (%)
NiO_x/PVSK/C_{60}	0.036	0.12	0.684
NiO_x/SAM/PVSK/C_{60}	0.025	0.116	0.643
SAM/PVSK/C_{60}	0.031	0.128	0.778
NiO_x/PVSK/PCBM	0.015	0.043	0.09
NiO_x/SAM/PVSK/PCBM	0.015	0.039	0.074
SAM/PVSK/PCBM	0.018	0.047	0.105

Table S5 PV parameters of the champion PCBM-based PSC under reverse and forward scans.

Devices	Scan direction	V_{OC} (V)	J_{SC} (mA/cm^2)	*FF* (%)	PCE (%)
Standalone PSC	Reverse	1.120	22.4	75.2	18.8
	Forward	1.117	22.3	74.5	18.6
PSC (coupled with HIT-n)	Reverse	1.120	21.7	78.2	19.0
	Forward	1.121	21.7	77.0	18.7
PSC (coupled with HIT-p)	Reverse	1.124	21.3	77.7	18.6
	Forward	1.128	21.5	76.3	18.5

Table S6 Short-wavelength light (300-760 nm) and long-wavelength light (760-1200 nm) utilization rates for sub-cells compared to solar spectrum

Devices	Short-wavelength light (300-760 nm) utilization rate (%)	Long-wavelength light (760-1200 nm) utilization rate (%)
PSC	84.98	2.00
HIT SSC	9.47	61.78

Table S7 A summary of 4-T perovskite/silicon tandem cells in literature.

Tandem architecture	PCE (%)	Structure of PSC	Substrate electrode	Top electrode	Type of SSC	Tandem side of SSC	Published year	Reference
Reflective tandem	27.6	Inverted	IWO	Ag	Bifacial HIT	Dual side	-	This work
	23.1	Normal	ITO	Au	IBC	Single side	2016	[8]
	23.1	Inverted	ITO	Ag	PERC	Single side	2017	[9]
	25.57	Normal	IWO	Au	Bifacial HIT	Dual side	2019	[10]
Mechanically stacked tandem	13.4	Normal	FTO	MoO_x/ITO	HIT	Single side	2015	[11]
	17.0	Normal	FTO	AgNW	mc-Si	Single side	2015	[12]
	18.18	Normal	FTO	MoO_x/IZO	HIT	Single side	2015	[13]
	18.0	Inverted	ITO	AZO/ITO	mono-Si	Single side	2016	[14]
	20.1	Normal	ITO	MoO_x/ITO	PERL	Single side	2016	[15]
	22.4	Normal	FTO	Solution ITO/Sputtered ITO	HIT	Single side	2016	[16]
	23.0	Inverted	ITO	Cu/Au	HIT	Single side	2016	[17]
	24.5	Normal	ITO	MoO3/ITO	IBC	Single side	2016	[18]
	25.2	Normal	ITO	MoO_x/IO:H/ITO	HIT	Single side	2016	[19]
	22.6	Normal	ITO	ITO	IBC	Single side	2017	[20]
	26.4	Normal	ITO	MoO_x/ITO	IBC	Single side	2017	[21]
	21.4	Normal	FTO	Au/ITO	HIT	Single side	2018	[22]
	19.2	Normal	n-PEDOT: PSS	n-PEDOT: PSS	mono-Si	Single side	2018	[23]
	21.18	Normal	FTO	ITO	Al-BSF	Single side	2018	[24]
	25.3	Normal	ITO	MoO_x/ITO	IBC	Single side	2018	[25]
	26.7	Inverted	ITO	AZO/AgNW	PERL	Single side	2018	[26]
	27.1	Normal	ITO	ITO/MgF_2	IBC	Single side	2018	[27]
	26.2	Inverted	IZrO	IZrO	HIT	Single side	2019	[28]
	26.7	Inverted	ITO	IZO	TOPCon	Single side	2019	[29]
	27.0	Normal	ITO	MoO_3/Au	HIT	Single side	2019	[30]
	26.5	Inverted	ITO	ITO	Bifacial HIT	Single side	2020	[31]
	27.7	Normal	ITO	MoO_x/IZO	IBC	Single side	2020	[32]
	28.6	Normal	IZrO	IZO	HIT	Single side	2020	[33]
	28.3	Normal	ITO	Cr/Au/MgF_2	HIT	Single side	2021	[34]

Supplementary References

1. A. Al-Ashouri, A. Magomedov, M. Roß, M. Jošt, M. Talaikis, G. Chistiakova, T. Bertram, J. A. Márquez, E. Köhnen and E. Kasparavičius, *Energy & Environmental Science*, 2019, **12**, 3356-3369.
2. L. Zheng and Y. Xuan, *Applied Energy*, 2021, **301**, 117496.
3. J. M. Ball, S. D. Stranks, M. T. Hörantner, S. Hüttner, W. Zhang, E. J. Crossland, I. Ramirez, M. Riede, M. B. Johnston and R. H. Friend, *Energy & Environmental Science*, 2015, **8**, 602-609.
4. M. I. Hossain, A. M. Hasan, W. Qarony, M. Shahiduzzaman, M. Islam, Y. Ishikawa, Y. Uraoka, N. Amin, D. Knipp and M. Akhtaruzzaman, *Small Methods*, 2020, **4**, 2000454.
5. J. Werner, G. Nogay, F. Sahli, T. C.-J. Yang, M. Brä uninger, G. Christmann, A. Walter, B. A. Kamino, P. Fiala and P. Lö per, *ACS energy letters*, 2018, **3**, 742-747.
6. M. Filipič, P. Löper, B. Niesen, S. De Wolf, J. Krč, C. Ballif and M. Topič, *Optics Express*, 2015, **23**, A263-A278.
7. A. Richter and J. Sturm, *Applied Physics A*, 1995, **61**, 163-170.
8. T. Duong, D. Grant, S. Rahman, A. Blakers, K. J. Weber, K. R. Catchpole and T. P. White, *Ieee Journal of Photovoltaics*, 2016, **6**, 1432-1439.
9. Y. Li, H. Hu, B. Chen, T. Salim, J. Zhang, J. Ding, N. Yuan and Y. M. Lam, *Journal of Materials Chemistry C*, 2017, **5**, 134-139.
10. L. Zheng, J. Wang, Y. Xuan, M. Yan, X. Yu, Y. Peng and Y.-B. Cheng, *Journal of Materials Chemistry A*, 2019, **7**, 26479-26489.
11. P. Löper, S.-J. Moon, S. M. De Nicolas, B. Niesen, M. Ledinsky, S. Nicolay, J. Bailat, J.-H. Yum, S. De Wolf and C. Ballif, *Physical Chemistry Chemical Physics*, 2015, **17**, 1619-1629.
12. C. D. Bailie, M. G. Christoforo, J. P. Mailoa, A. R. Bowring, E. L. Unger, W. H. Nguyen, J. Burschka, N. Pellet, J. Z. Lee and M. Grätzel, *Energy & Environmental Science*, 2015, **8**, 956-963.
13. J. Werner, G. Dubuis, A. Walter, P. Löper, S.-J. Moon, S. Nicolay, M. Morales-Masis, S. De Wolf, B. Niesen and C. Ballif, *Solar Energy Materials and Solar Cells*, 2015, **141**, 407-413.
14. K. A. Bush, C. D. Bailie, Y. Chen, A. R. Bowring, W. Wang, W. Ma, T. Leijtens, F. Moghadam and M. D. McGehee, *Advanced Materials*, 2016, **28**, 3937-3943.
15. T. Duong, N. Lal, D. Grant, D. Jacobs, P. Zheng, S. Rahman, H. Shen, M. Stocks, A. Blakers and K. Weber, *Ieee Journal of Photovoltaics*, 2016, **6**, 679-687.
16. D. P. McMeekin, G. Sadoughi, W. Rehman, G. E. Eperon, M. Saliba, M. T. Hörantner, A. Haghighirad, N. Sakai, L. Korte and B. Rech, *Science*, 2016, **351**, 151-155.
17. B. Chen, Y. Bai, Z. Yu, T. Li, X. Zheng, Q. Dong, L. Shen, M. Boccard, A. Gruverman and Z. Holman, *Advanced Energy Materials*, 2016, **6**, 1601128.
18. J. Peng, T. Duong, X. Zhou, H. Shen, Y. Wu, H. K. Mulmudi, Y. Wan, D. Zhong, J. Li and T. Tsuzuki, *Advanced Energy Materials*, 2017, **7**, 1601768.
19. J. Werner, L. Barraud, A. Walter, M. Brä uninger, F. Sahli, D. Sacchetto, N. Tétreault, B. Paviet-Salomon, S.-J. Moon and C. Allebé, *ACS energy letters*, 2016, **1**, 474-480.
20. M. Jaysankar, W. Qiu, M. van Eerden, T. Aernouts, R. Gehlhaar, M. Debucquoy, U. W. Paetzold and J. Poortmans, *Advanced Energy Materials*, 2017, **7**, 1602807.
21. T. Duong, Y. Wu, H. Shen, J. Peng, X. Fu, D. Jacobs, E. C. Wang, T. C. Kho, K. C. Fong and M. Stocks, *Advanced Energy Materials*, 2017, **7**, 1700228.
22. H. Kanda, N. Shibayama, A. Uzum, T. Umeyama, H. Imahori, K. Ibi and S. Ito, *ACS applied materials & interfaces*, 2018, **10**, 35016-35024.

23. Y. Zhang, Z. Wu, P. Li, L. K. Ono, Y. Qi, J. Zhou, H. Shen, C. Surya and Z. Zheng, *Advanced Energy Materials*, 2018, **8**, 1701569.
24. F. J. Ramos, S. Jutteau, J. Posada, A. Bercegol, A. Rebai, T. Guillemot, R. Bodeux, N. Schneider, N. Loones and D. Ory, *Scientific Reports*, 2018, **8**, 1-11.
25. M. Jaysankar, M. Filipič, B. Zielinski, R. Schmager, W. Song, W. Qiu, U. W. Paetzold, T. Aernouts, M. Debucquoy and R. Gehlhaar, *Energy & Environmental Science*, 2018, **11**, 1489-1498.
26. C. O. R. Quiroz, Y. Shen, M. Salvador, K. Forberich, N. Schrenker, G. D. Spyropoulos, T. Heumüller, B. Wilkinson, T. Kirchartz and E. Spiecker, *Journal of Materials Chemistry A*, 2018, **6**, 3583-3592.
27. M. Jaysankar, B. A. Raul, J. Bastos, C. Burgess, C. Weijtens, M. Creatore, T. Aernouts, Y. Kuang, R. Gehlhaar and A. Hadipour, *ACS energy letters*, 2018, **4**, 259-264.
28. E. Aydin, M. De Bastiani, X. Yang, M. Sajjad, F. Aljamaan, Y. Smirnov, M. N. Hedhili, W. Liu, T. G. Allen and L. Xu, *Advanced Functional Materials*, 2019, **29**, 1901741.
29. A. Rohatgi, K. Zhu, J. Tong, D. H. Kim, E. Reichmanis, B. Rounsaville, V. Prakash and Y.-W. Ok, *Ieee Journal of Photovoltaics*, 2020, **10**, 417-422.
30. Z. Wang, X. Zhu, S. Zuo, M. Chen, C. Zhang, C. Wang, X. Ren, Z. Yang, Z. Liu and X. Xu, *Advanced Functional Materials*, 2020, **30**, 1908298.
31. G. Coletti, S. L. Luxembourg, L. Geerligs, V. Rosca, A. Burgers, Y. Wu, L. Okel, M. Kloos, F. Danzl and M. Najafi, *ACS energy letters*, 2020, **5**, 1676-1680.
32. T. Duong, H. Pham, T. C. Kho, P. Phang, K. C. Fong, D. Yan, Y. Yin, J. Peng, M. A. Mahmud and S. Gharibzadeh, *Advanced Energy Materials*, 2020, **10**, 1903553.
33. B. Chen, S.-W. Baek, Y. Hou, E. Aydin, M. De Bastiani, B. Scheffel, A. Proppe, Z. Huang, M. Wei and Y.-K. Wang, *Nature Communications*, 2020, **11**, 1-9.
34. D. Yang, X. Zhang, Y. Hou, K. Wang, T. Ye, J. Yoon, C. Wu, M. Sanghadasa, S. F. Liu and S. Priya, *Nano Energy*, 2021, **84**, 105934.